Structure and Kinematics of the Milky Way through A stars

Author: Judith Ardèvol Guillamón

Advisor: Maria Monguió Montells

June 2022

UNIVERSITAT DE
BARCELONA

Abstract

In the context of the Gaia era, the analysis of the structure and the kinematics of the Milky Way is an ongoing active field of research. Despite A-type stars have a relatively high intrinsic brightness and are moderately numerous as well as kinetically cold, they have been scarcely used as tracers of Galactic properties.

This work opens a new window by studying a sample of A-type stars selected using the IGAPS photometric survey. It covers the Galactic plane within $30\,^\circ \leq l \leq 215\,^\circ$ and $|b| \leq 5\,^\circ$ up to magnitude $r \leq 19\,\mathrm{mag}$ with around 3.5 million sources. *Gaia* EDR3 astrometry and proper motions, together with *Gaia* DR3 line-of-sight velocities, are used to analyse large-scale features of the Galactic disc.

This sample allows to unveil structure and kinematic properties of the Milky Way disc at intermediate stellar ages. This includes a study of the obtained density distributions completeness, and a comparison between the $b < 0^\circ$ and $b > 0^\circ$ regions. Furthermore, the sample shows clear evidences of the Galactic warp in its vertical kinematics. Possible biases caused by interstellar extinction or by the usage of some kinematic estimators are examined to verify the results.

The last goal of this study is to demonstrate the high potential of A-type stars as Galactic-scale tracers. They can be used to fill the age gap between the youngest OB stars and the old red giants, allowing to expand our knowledge about the evolution of the Galaxy.

Contents

1 Introduction

Our knowledge about the Milky Way has been extremely improved in the last decades. Despite this, there are still many unknowns to be deciphered. Our location inside the Galaxy makes it more difficult to detect its structure in comparison with the rest of the galaxies that are seen from outside. By contrast, our advantaged position allows us to analyse our own Galaxy with a very high level of detail. In turn, this enables the study of density and kinematic peculiar patterns produced by non-axisymmetric features (such as spiral arms) or by external perturbations.

The *Gaia* mission (Gaia Collaboration et al. 2016) has helped us to learn more about previously observed properties of the Milky Way, as well as to discover other non-equilibrium structures (e.g., Antoja et al. 2018; Belokurov et al. 2018; Helmi et al. 2018, among many others). As an example, Gaia Collaboration et al. (2021a) and McMillan et al. (2022) demonstrated that *Gaia* measurements are able to highlight large non-equilibrium features of the Milky Way.

The huge amount of data it has already produced, together with its high quality, make it ideal to analyse the structure of our Galaxy. Nevertheless, on-ground photometric and spectroscopic surveys are also extremely valuable to complement –or to be complemented by– *Gaia* data. In particular, these additional observations can be the photometry of IGAPS (Monguió et al. 2020) or the spectra that will be obtained with WEAVE (Dalton 2016) –whose first light is expected to occur this summer–, together with a very long list of possibilities.

A multi-tracer study of the Milky Way allows us to disentangle its structure and kinematics within a wide range of ages and so, to examine their evolution. Some of the more widely used Galactic tracers are interstellar gas and dust, open clusters, young OB stars or old red giants, among others.

As a non-exhaustive list of authors that have analysed the Galactic structure, Poggio et al. (2021) used very young tracers (Upper Main Sequence stars, Cepheids and open clusters) and find high-density structures associated with spiral arms. Pantaleoni González et al. (2021) made use of massive OB stars and stressed the presence of a coherent feature that they called Cepheus Spur. In comparison, Cantat-Gaudin et al. (2020) constructed their own catalogue of open clusters to examine which structures they trace, concluding that their distribution is highly dependent on their age, and that the oldest ones present signatures of both Galactic warp and flare. The Galactic warp has also been examined, for instance, with Cepheids (Chen et al. 2019) or with young OB and old Red Giant Branch (RGB) stars (Romero-Gómez et al. 2019).

Using tracers with different stellar ages is key to understand the evolution of the Milky Way (Amôres et al. 2017). Since intermediately young A-type stars are relatively intrinsically bright and numerous, they are suitable for tracing density structures in the Galactic disc. They are young enough to have small velocity dispersion, being at the same time old enough to trace kinematic perturbations. Therefore, they are also appropriate for kinematic studies.

In fact, these tracers open a new window to understand the Milky Way disc by offering the best of the two most frequently used types of tracers; namely, the brightness of giants and Upper Main Sequence stars, the low velocity dispersion of young stars and the relatively high abundance of cooler stars.

Despite all these strengths, these targets have been historically relegated from the list of common tracers in favour of some of the aforementioned ones. A few examples of research already performed with these stars are Drew et al. (2008), Sale et al. (2010), Monguió et al. (2015) or Harris et al. (2018, 2019).

The aim of this work is to highlight the role of A-type stars to perform Galactic-scale studies. The capability of reaching so large scales with these targets is possible thanks to the usage of colour-colour diagrams for their selection, which have two main advantages. First, they are feasible for a very large number of stars as they enable spectral classifications only based on photometry rather than on spectroscopy. Second, the utilisation of a specific combination of colours allow to perform the selection without correcting a Hertzsprung-Russell diagram and so, avoiding uncertainties and degeneracy derived from distances and extinction.

This report is structured as follows. Section 2 defines the nomenclature and the symbols used throughout the work while Section 3 describes the data and different samples used. The analysis of stellar densities and Galactic structures is performed in Section 4, both across the XY plane (Subsection 4.2) and in the vertical direction (Subsection 4.3). The employed methods are described in Subsection 4.1. Section 5 explores the biases produced by the shortage of line-of-sight velocities (Subsection 5.1) and describes the kinematic properties of the sample (Subsections 5.2 and 5.3). A discussion of obtained results and comparisons with the literature are developed in Section 6. Lastly, Section 7 summarizes the results and presents the conclusion of the work.

2 Nomenclature, definitions and reference systems

This section is devoted to define the most used variables, the symbols representing them and their numerical value when applicable.

On the one hand, the photometric bands used

are r, $H\alpha$ and i, which are centered at 624.0, 656.8 and 774.3 nm, respectively. Parallaxes and their uncertainties are denoted by ϖ and $\delta\varpi$. The distance between a star and the Sun is indicated with d.

On the other hand, several reference systems are utilised in this work. The spherical heliocentric system is defined by right ascension, declination and distances (α, δ, d), along with equatorial proper motions (μ_α, μ_δ) and line-of-sight velocities $\mathrm{v_{los}}$. Proper motion in the right ascension direction already contains the cosine term of the declination that accounts for projection effects; that is, $\mu_\alpha = \mu_\alpha^{observed}\, cos(\delta)$.

This system can be transformed into the Galactic system, which is also centered at the Sun. It is described by (l, b, d) and (μ_l, μ_b, $\mathrm{v_{los}}$), where the first two variables correspond with Galactic longitude and Galactic latitude, respectively, and (μ_l, μ_b) represent proper motions in these directions. As in the previous case, projection effects are already considered so that $\mu_l = \mu_l^{observed}\, cos(b)$.

Velocities in these Galactic directions are called ($\mathrm{v_l}$, $\mathrm{v_b}$) and are computed according to:

$$\mathrm{v}_\gamma^{\mathrm{uncorr}} = 4.7404705\, d\, \mu_\gamma \quad \text{with } \gamma = l, b \qquad (1)$$

where $\mathrm{v}_\gamma^{\mathrm{uncorr}}$ is in km/s provided that d is in kpc and μ_γ, in mas/yr.

Both velocities given by Eq. (1), as well as $\mathrm{v_{los}}$, are corrected for solar motion with:

$$\begin{aligned} \mathrm{v_l^{corr}} &= \mathrm{v_l^{uncorr}} - \mathrm{U_\odot sin(l) + V_\odot cos(l)} \\ \mathrm{v_b^{corr}} &= \mathrm{v_b^{uncorr}} - \mathrm{U_\odot cos(l) sin(b)} \\ &\quad \mathrm{-V_\odot sin(l) sin(b) + W_\odot cos(b)} \end{aligned} \qquad (2)$$

$$\begin{aligned} \mathrm{v_{los}^{corr}} &= \mathrm{v_{los} + U_\odot cos(l) cos(b)} \\ &\quad \mathrm{+V_\odot sin(l) cos(b) + W_\odot sin(b)} \end{aligned} \qquad (3)$$

where ($\mathrm{U_\odot}$, $\mathrm{V_\odot}$, $\mathrm{W_\odot}$) are the customary components of the solar motion. $V_\odot$ includes both the circular velocity of the Local Standard of Rest (LSR) and the peculiar azimuthal velocity of the Sun with respect to it (Abedi 2015; Harris et al. 2019; Gaia Collaboration et al. 2021a).

Heliocentric Cartesian coordinates are named with capital X, Y and Z, whereas Galactocentric ones are distinguished with a subscript: X_{Gal}, Y_{Gal} and Z_{Gal}. Their transformations are $X = X_{Gal} + \mathrm{R_\odot}$ and $Z = Z_{Gal} + \mathrm{Z_\odot}$, while the Y component of both reference systems coincide. The values of the solar radius, $\mathrm{R_\odot}$, and its vertical position, $\mathrm{Z_\odot}$, are defined in the last paragraph of this section. Both sets of axes define a right-handed system where X increases towards the Galactic Centre (GC) for the heliocentric case or away from the Sun for the Galactocentric one. In either case, Y grows in the direction that rotation has for $X_{Gal} < 0$ and Z, towards the North Galactic Pole (NGP).

Cylindrical Galactocentric radial, azimuthal and vertical coordinates are referred to as R, ϕ and $\mathrm{Z_{Gal}}$; while the respective velocities are $\mathrm{V_R}$, V_ϕ and $\mathrm{V_Z}$. (R, ϕ, Z) define a left-handed system in which R increases away from the GC and ϕ originates at the Sun-Anticentre direction. The angle increases clockwise as seen from the NGP, towards which $\mathrm{Z_{Gal}}$ grows. In the case of the three velocities: $\mathrm{V_R}$ is positive outwards; V_ϕ, in the direction of rotation (clockwise from the NGP) and $\mathrm{V_Z}$, towards the NGP.

The used distance between the Sun and the GC is equal to $\mathrm{R_\odot} = 8.249 \pm 0.009$ kpc (Gravity Collaboration et al. 2020) while the solar vertical coordinate $\mathrm{Z_\odot}$ is assumed to be zero as a simplifying approximation (so, $Z = Z_{Gal}$). The solar motion is taken from Drimmel & Poggio (2018) [$\mathrm{U_\odot}$] and Reid & Brunthaler (2020) [$\mathrm{V_\odot}$ and $\mathrm{W_\odot}$]. It equates to ($\mathrm{U_\odot}$, $\mathrm{V_\odot}$, $\mathrm{W_\odot}$) = (9.5, 250.7, 8.56) km/s once scaled to the aforementioned $\mathrm{R_\odot}$.

3 Data

IGAPS is a photometric survey covering the northern Galactic plane within $l \in [30\,,\,215]^\circ$ and $|b| \leq 5^\circ$ in five optical bands: i, r, $H\alpha$, g and U_{RGO}. It contains two measurements for the r band, one from IPHAS (Drew et al. 2005) and one for UVEX (Groot et al. 2009). The former is the reference magnitude in this work.

This survey allows to select A-type stars in a considerably efficient way employing the $(r - H\alpha)$ vs $(r - i)$ colour-colour diagram with a procedure similar to that described in Drew et al. (2008). In fact, Sale et al. (2010) and Harris et al. (2018) found only about $10 - 20\%$ of contamination in their selections, which use very similar methodologies.

To obtain the sample of this work, the first step was to remove noise-like sources with Class!=0. Second, white dwarfs and supergiants were avoided by imposing that $-0.1 < (r - i) < 2.2$. Then, stars of types A0-A5 were selected according to

$$\begin{aligned} (r - H\alpha) - (\delta r - \delta H\alpha) & \\ -[0.0032 & \\ +0.3735(r - i) & \\ -0.0608(r - i)^2 & \\ +0.0041(r - i)^3] &< 0, \end{aligned} \qquad (4)$$

which accounts for the uncertainties in the $(r - H\alpha)$ colour. A sample with 19 195 804 stars is obtained with this process.

As the selection has proven to be not reliable for the faintest stars[1], the limit $r \leq 19$ mag was also

[1]The expected trend in the $\delta\varpi/\varpi$ vs r plot for a sample having a narrow range in absolute magnitude like this one is to be smoothly increasing. By contrast, those sources fainter than $r = 19$ mag do not follow the expected trend as they have extremely large dispersion in the $\delta\varpi/\varpi$ axis.

applied to the sample, which reduced it to 3 532 751 stars (18.4%).

Parallaxes and proper motions (μ_α, μ_δ) were then obtained from *Gaia* EDR3 (Gaia Collaboration et al. 2021b). For this, the sample was cross-matched with this catalogue utilising a 1" radius. This gave 3 515 778 counterparts (99.5% of stars brighter than $r = 19$ mag), out of which 3 494 290 (98.9% of the same group) have the three quantities of interest. However, only 1 652 of them have line-of-sight velocities from *Gaia* DR2 (strictly speaking, v_{los} included in *Gaia* EDR3 are from DR2). 3 303 880 sources (94.5% of stars with astrometry) have $RUWE < 1.4$.

As a value-added result, the IGAPS list containing A0-A5 stars up to $r = 19$ mag has also been cross-matched, using the same radius as before, with *Gaia* DR3 (Gaia Collaboration et al. 2022b, Gaia Collaboration et al. (2022k) *in prep.*[2]) –released on 13 June this year–, with the objective of adding line-of-sight velocities to the sample. There are 32 032 sources (0.9%) with available v_{los}. It is worth to notice that they have a magnitude limit of $G_{RVS} = 14$ mag. These line-of-sight velocities has been corrected according to Katz et al. (2022), which provides a small correction for this sample always below 0.4 km/s. The correction described by Blomme et al. (2022) is not applied since most of the stars did not match the requirements for it.

Utilising the best possible distance estimator is key for this work as its goal is to unveil large-scale density and kinematic structures of the Milky Way. This is why I compared several estimators; namely, $1/\varpi$, the two distances from Bailer-Jones et al. (2021) and the mode of EDSD[3] priors with different length scales (i.e., L = 1, 2, 2.5 and 3 kpc).

It is widely known that $1/\varpi$ presents strong biases (e.g., Bailer-Jones 2015; Luri et al. 2018). Furthermore, the Bailer-Jones et al. (2021) estimator using a photometric prior is not so well-behaved for our relatively blue stars lying near the Galactic plane (where extinction effects can be relevant) than for colder, more numerous stars. The dependence in direction of the length scale used in their geometric estimator complicates the determination of the effect of the prior on the derived distances.

Thus, distances in this work are computed with the one-parameter EDSD prior, which rely in a very small number of assumptions. Specifically, the length scale L = 3 kpc seems to be more appropriate for a sample of A0-A5 stars. However, it should be taken into account that any distance estimator includes biases for parallaxes with large errors. In particular, the selected one tends to accumulate these stars at a distance equal to twice the length scale (i.e., at 6 kpc from the Sun in this case). In consequence, the presence of any buildup at this particular distance should be suspicious. Furthermore, results at distances beyond 6 kpc may be considerably affected by the prior and are not completely reliable.

To mitigate the effects of large parallax errors, a cut in $\delta\varpi/\varpi$ can be applied. As stated by Luri et al. (2018), the usage of this type of quality cuts derives in a biased sample. Furthermore, when imposing $0 \leq \delta\varpi/\varpi \leq 30\%$[4] to the sample combining both IGAPS and Gaia EDR3 (see above), the loss of stars begins at $d \approx 1$ kpc. So, the completeness of almost the full sample may be affected. The removal of negative parallaxes also biases this alternative sample. However, all stars having $\varpi < 0$ lay beyond $d = 6$ kpc when using the ESDS estimator with a length scale L = 3 kpc. Thus, the null lower limit does not affect the derived results for $d \leq 6$ kpc. From now on, this reduced sample containing higher-quality parallaxes will be referred to as the pP30 sample. It contains 1 395 533 sources.

An analogous sample, hereinafter named pP30-DR3RV, has also been created following the same procedure but for those stars having v_{los} from the newest *Gaia* data release. That is, applying the cut $0 \leq \delta\varpi/\varpi \leq 30\%$ to the cross-match between the IGAPS list of A0-A5 stars up to $r = 19$ mag and the DR3 stars having line-of-sight velocity. This sample reaches shorter distances than the previous one (up to $d \sim 3$ kpc rather than $d \sim 5 - 6$ kpc) because of the $G_{RVS} = 14$ mag limiting magnitude imposed to *Gaia* DR3 line-of-sight velocities. The majority of stars with v_{los} in DR3 (more than 94% of them) belong to this sample.

Last, the less restrictive $0 \leq \delta\varpi/\varpi \leq 50\%$ quality cut is utilised to construct the pP50 and pP50-DR3RV samples (named in analogy with the previous pP30 and pP30-DR3RV designation).

4 Structure

This section describes two procedures that shed light on the Milky Way structure through the analysis of stellar densities across the Galactic plane. In addition, it studies the vertical distribution of stars by comparing the sample above and below the plane defined by $b = 0°$.

[2] https://doi.org/10.1051/0004-6361/202243940

[3] EDSD stands for Exponentially Decreasing Space Density. This prior assigns the probability $P(d|L) = (d^2 e^{-d/L})/(2L^3)$ to any distance $d > 0$, while it is null for $d \leq 0$. It can be combined with the likelihood of the parallax given d and $\delta\varpi$ in a Bayesian approach to estimate distances from ϖ and its uncertainty for a given scale L. See for instance Bailer-Jones (2015) or Astraatmadja & Bailer-Jones (2016) for a more detailed description and analysis.

[4] The 30% upper limit has been chosen among several studied values as a compromise between removing as much as distance uncertainty as possible and avoiding being too restrictive at the same time. Around 70% of stars are still preserved up to 3 kpc after this cut.

4.1 Methods

4.1.1 Surface density

Since the sample is limited on Galactic latitude, the volume it covers increases with the distance to the Sun. One way to take this into account is to discretize the (l, d) plane into a grid of size ($2\delta l$, Δd) and count the number of stars inside each bin, N. The stellar volume density is obtained by dividing N/V, where V is given by

$$V = \frac{4}{3}\tan(\delta \mathrm{b})\tan(\delta \mathrm{l})[(\mathrm{d}+\Delta \mathrm{d})^3 - \mathrm{d}^3]. \quad (5)$$

Figure 1 shows the scheme of the described configuration.

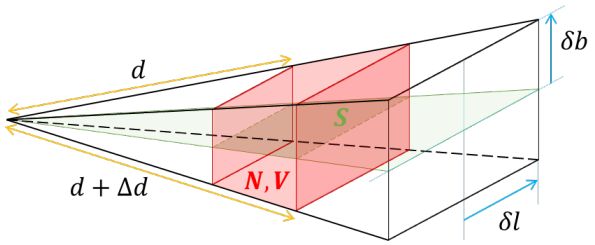

Fig. 1: Volume occupied by a slice in l of the sample (black pyramid) with the Sun at the left vertex. The red truncated pyramid defines a bin (within the distance interval d, $d+\Delta d$ and having $2\delta l$ width in l) which has volume V and contains N stars. The green surface labeled with an S is the area over the Galactic plane ($b = 0°$) that is associated with this bin in distance and Galactic longitude.

This method provides the mean density inside each bin, but it has a relevant issue. As it just averages the density through a given volume, it does not account for the fact that the number of stars diminishes when getting away from the Galactic plane (with increasing $|Z_{Gal}|$). The bins nearest to the Sun only sample denser regions (near $Z_{Gal} = 0$), whereas the furthest ones may also include less-crowded regions outside the Galactic disc. In consequence, this methodology has an intrinsic bias for a b-limited sample, in the sense that densities tend to be underestimated at large distances.

To correct this effect, one can use surface densities instead of volume ones. The required procedure is described next.

Firstly, a certain vertical distribution must be assumed for stars of the Galactic disc (van der Kruit & Searle 1981):

$$\mathcal{N}(Z) = \frac{1}{2h_Z}\,\mathrm{sech}^2\left(\frac{\mathrm{Z}}{\mathrm{hz}}\right) \quad \mathrm{Z} \in (-\infty, \infty), \quad (6)$$

where the assumed scale height h_Z is 200 pc for A0-A5 stars (see section 4.1 from Monguió et al. 2015, and references therein).

Secondly, the method requires the knowledge of the fraction of the vertical axis that is sampled when considering stars covering the range (b_{min}, b_{max}), which translates into a given Z range (Z_{min}, Z_{max}) with Eq. (8):

$$\begin{aligned} f &= \int_{Z_{min}}^{Z_{max}} \mathcal{N}(Z)\,dZ = \\ &= \frac{1}{2}\left[\tanh\left(\frac{Z_{max}}{h_Z}\right) - \tanh\left(\frac{Z_{min}}{h_Z}\right)\right] \end{aligned} \quad (7)$$

Using the same intervals as defined in Fig. 1 and assigning the final result to the midpoint of each bin (at distance $d + \Delta d/2$) leads to

$$Z_m = [d + \Delta d/2]\tan(b_m) \quad (8)$$

where the subscript m stands for min or for max.

Thirdly, the number of stars counted inside each bin is adjusted to determine the total number of them inside a bin analogous in l and d, but having infinite height: $N_{tot} = N/f$. Lastly, the surface density is computed as $\Sigma = N_{tot}/S$, where S is the area of the bin projected onto the Galactic plane (see Fig. 1):

$$S = [(d + \Delta d)^2 - d^2]\,\delta l \quad (9)$$

with δl in radians.

This last step accounts for the increase of the area over the Galactic plane with distance, which derives from the slice in Galactic longitude.

4.1.2 Kernel overdensities

An alternative approach to locate Galactic structures from a catalogue of stars is to compute stellar over(under)densities via a Bivariate kernel density estimation. Although this method cannot provide the absolute scale of the densities, it is better to highlight local overdensities. In fact, they are enhanced by this second method at larger distances –where absolute densities are lower–, while partially hidden in the Poisson noise when computing surface densities.

The basics of this method rely on computing a mean stellar density (Σ_{mean}) and a local one (Σ_{local}) for a grid of points in the XY plane. The former involves a bigger volume than the latter thanks to the use of a larger spatial scale (i.e., a larger bandwidth). The overdensity of each point (X_0, Y_0) is computed according to:

$$\begin{aligned} \Delta_\Sigma(X_0, Y_0) &= \frac{\Sigma_{local}(X_0, Y_0) - \Sigma_{mean}(X_0, Y_0)}{\Sigma_{mean}(X_0, Y_0)} \\ &= \frac{\Sigma_{local}(X_0, Y_0)}{\Sigma_{mean}(X_0, Y_0)} - 1. \end{aligned} \quad (10)$$

See Appendix B.1 from Poggio et al. (2021) and the reference therein for a more detailed explanation on how Σ_{mean} and Σ_{local} are obtained from a given Kernel function (the Epanechnikov one in this work).

This method has some edge effects that are mainly originated at both l limits. They can be partially corrected by taking into account which is the real sampled area. However, the outermost values

are still less trustworthy because of the low statistics in these regions.

4.2 Density in the XY plane

The surface-density map in the XY plane of the Galaxy resulting from the methodology explained in Section 4.1.1 is show in Fig. 2. Densities are very uncertain for $d \leq 0.5\,\mathrm{kpc}$ as they rely in a very low number of stars owing to the small volume covered ($f < 0.2$). Therefore, they are not shown.

The parameters that define the grid are: $\delta l = 1°$, $\Delta d = 100\,\mathrm{pc}$. For now, there is no cut in the vertical direction; that is, $b_{min} = -5°$ and $b_{max} = 5°$ in Eq. (7-8). Section 4.3 goes one step further comparing data form $b > 0°$ and from $b < 0°$.

Two evident features in Fig. 2 are the high density values visible at $(X, Y) \approx (-1.75, 1.75)\,\mathrm{kpc}$ and around $(X, Y) \approx (0.5, 1.5)\,\mathrm{kpc}$, which are respectively associated to the Perseus arm and the Cygnus region. In addition, it presents obvious trends in the radial direction with respect to the Sun that are not real features of the Galaxy.

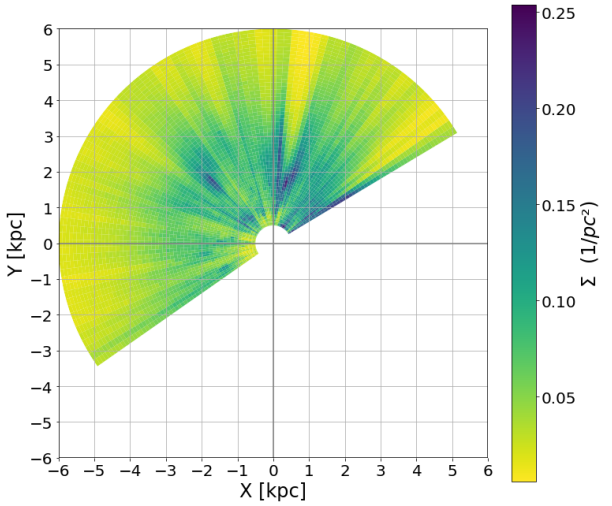

Fig. 2: Heliocentric XY map of the stellar surface density limited to $d \leq 6\,\mathrm{kpc}$. See text for more details about grid parameters. The Sun is located at the origin and the GC is at $X = \mathrm{R}_\odot$, beyond the right-hand edge of the plot. Galactic longitude grows counterclockwise starting from the Sun-GC line.

These radial characteristics can have two basic origins: extinction and distance uncertainties. On the one hand, they can be cones of low density caused by foreground extinction (as the light yellow triangular region beyond Cygnus *over*density). As absorption fades background stars, the number of them that can be detected diminishes. Consequently, stellar density seems to drop behind high-extinction regions. On the other hand, large parallax uncertainties translate into large distance uncertainties. As a result, stars positions are unsure and the surface density becomes blurred in the radial direction (this is the case for all, or mostly, of the darker stripes further than $d \approx 4\,\mathrm{kpc}$). This second effect elongates density structures, which appear distorted even if they are real.

Dealing with these two artefacts is not straightforward. A 3D extinction map is required to estimate the consequences of the former, whereas the latter may be mitigated by restricting the sample to high-quality parallaxes (i.e., imposing a limiting value for $\delta\varpi/\varpi$). The extinction effects will be addressed in Section 4.2.1.

To avoid the impact of the distance uncertainties, the pP30 sample (defined in Section 3) is used from now on except when otherwise stated. A given density structure obtained with this sample will be reliable if it is also detected with the previous one. The main benefit of performing a cut in $\delta\varpi/\varpi$ (between 0 and 30% in this case) is that the obtained density pattern is noticeably clearer, and certainly devoid of radial blurring. Consequently, the revealed structure is better defined and one can rely more in the shapes that are obtained.

The surface-density map resulting from applying the same method (section 4.1.1) to the pP30 sample is shown in Fig. 3. The framework of the obtained density pattern is basically the same as that in Fig. 2, which has no cut in parallax. The residuals between both figures are essentially radial with respect to the Sun. This confirms that discarding stars with highly-uncertain parallaxes can be an acceptable procedure provided that results are carefully validated (e.g., comparing with different samples and cuts or with simulations).

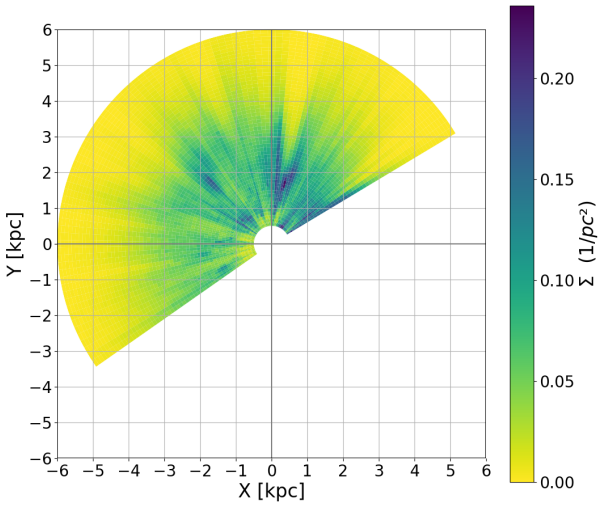

Fig. 3: The same as in Fig. 2 but with the pP30 sample (containing approximately 40% of the stars from Fig. 2).

Besides the two density features already detected in Fig. 2, Fig. 3 accentuates four additional structures that are only moderately visible in the previous one. Globally, its six principal points are:

a) The $(X, Y) \approx (-1.75,\, 1.75)$ kpc high density linked with the Perseus arm. Using this reduced sample, the presence of a second peak at $(X, Y) \approx (-1.75,\, 2.5)$ kpc is more prominent.

b) The "V" shape of the Cygnus region between $(X, Y) \approx (0,\, 1)$ kpc and $(X, Y) \approx (0.75,\, 2)$ kpc is emphasised. A feature near the Y axis and almost parallel to it between $Y \approx 2 - 3.5$ kpc is shown as well.

c) A denser band at $(X, Y) \approx (-0.75,\, 0.75)$ kpc, very near to the Sun ($d \approx 1$kpc) in the second quadrant.

d) A low-density elongated zone centered at $(X, Y) \approx (-1.75,\, 0.5)$ kpc.

e) Three small peaks relatively close to the Anti-centre (AC). In particular, two of them are on both sides of the $Y = 0$ line at $X \approx -1.5$ kpc and $X \approx 2$ kpc respectively. The third one is located at $(X, Y) \approx (-1.5,\, -0.75)$ kpc.

f) The beginning of a high-density section at the lower-l end of the sample (i.e., at the left radial cut of the XY maps) that extends up to $d \approx 3$ kpc.

Fig. 4 shows stellar overdensities computed following the method described in Section 4.1.2 with a local density bandwidth $h_{local} = 0.3$ kpc and a mean density bandwidth $h_{mean} = 1.5$ kpc. These overdensities are computed at intervals of 100pc in the X and the Y coordinates. It also employs the pP30 sample to avoid strong radial features.

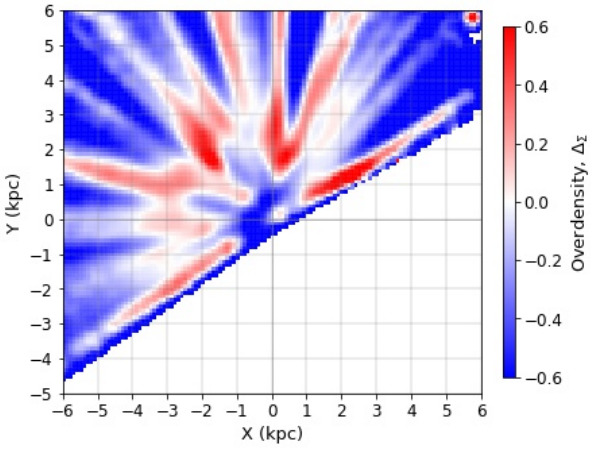

Fig. 4: Heliocentric XY map of stellar overdensities for the pP30 sample. The map for the initial sample is almost entirely radial and provides no information. The configuration of the plot is the same as in Fig. 2. See text for more details about grid parameters.

Results from the nearest ($d \lesssim 1$ kpc) region are not reliable because of the small volume of the sample. So they are the furthest values given the parallax uncertainties.

This figure displays the most prominent features from both Fig. 2 and 3; namely, those labeled with a), b) and d), along with the second and maybe the third[5] peaks in e). This allows to verify the results from the $0 \leq \delta\varpi/\varpi \leq 30\%$ cut with two different techniques.

On the other hand, Fig. 4 show a more radial pattern than Fig. 3, although they use the same sample. In fact, extinction and distance errors have more critical impact on this method than on surface densities. This is because the latter are only affected in the d direction, whereas the values from the former depend on all their vicinity (not only in d, but also in l).

Consequently, the lack of stars due to an isolated high-extinction region would create both an underdensity ($\Delta_\Sigma < 0$) region behind it, as well as two overdensities ($\Delta_\Sigma > 0$) along both sides of it. This secondary effect is caused for the sole reason that these points are compared with a region having less sources, and may not be associated with a real increase of stars. The opposite happens around radial overdensities created by distance uncertainties. Their combination results in very complex biases.

In summary, the second method that has been studied (computing overdensities using Kernel functions) is not extremely suitable for the sample, although it recovers the principal features found in Fig. 2 and in Fig. 3.

4.2.1 Completeness distance of the sample

When dealing with densities, it is important to take into account which effects exclude stars from being counted. In other words, it is necessary to establish up to which extend a sample can be considered complete, and from where stars begin to be lost owing to the combination of limiting magnitude and absorption. This section describes a method to estimate the sample completeness.

The apparent magnitude for a star at a given distance, taking into account the extinction (A_r), is:

$$r = M_r + log_{10}(d_{[pc]}) - 5 + A_r, \qquad (11)$$

where M_r is the absolute magnitude in the r-band ($M_r = 0.795$ mag and $M_r = 1.844$ mag respectively for A0 and A5 stars). Having a representative value of the extinction at each direction and distance is also needed to calculate r.

A_r values from Sale et al. (2014) and Green et al. (2019) extinction maps have been compared, leading to similar results. In general, the values of the former

[5] As the $(X, Y) \approx (-1.5,\, -0.75)$ kpc peak is so close to the edge, it is not possible to guarantee whether it is a real structure or not. The same happens for the f) structure.

are slightly lower. However, they are compatible at 1σ level and their difference never exceed half a magnitude. This study employs the first one. The more recent dust map from Lallement et al. (2022) has not been studied because it is limited to $d = 3$ kpc while the pP30 sample can reach deeper values of d. So, it would not have allowed the kind of analysis that has been performed.

Once M_r and $A_r(l, b, d)$ are established, the distance (d_{lim}) that can be reached for a limiting magnitude $r_{lim} = 19$ mag can be computed from Eq. (11) by isolating d. Nevertheless, this is not a one-to-one relation because of the presence of uncertainties and the finite resolution of extinction maps. Values of d_{lim} for the pP30 sample split into two vertical bins ($b < 0°$ and $b > 0°$) are shown in Fig. 5 as orange and blue lines.

This procedure gives d_{lim} values that roughly agree with distances at which dark features become yellowish in Fig. 3 except for $l \gtrsim 135°$. At these Galactic longitudes near the AC, they become much larger than 6 kpc, where the extinction map is no longer reliable according to their authors (Sale et al. 2014). Another caveat concerning this simple estimation of the sample completeness is that it works for magnitude-limited samples, but it is no longer valid for a sample with additional cuts (e.g., some $\delta\varpi/\varpi$ restrictions). In this second case, the determination of completeness limits becomes much more complex.

One approach to address repercussions of any selection or quality cut applied to the sample is to estimate the real percentage of stars lost after each of them. The idea of this perspective is to determine, for each direction and distance, a correction factor from a mock catalogue. This will allow to quantify up to which extend the biases derived from successive reductions of the sample affects the stellar density results. This better determination of the completeness limits of the different samples in a more precise and quantitative way is planned to be done in the near future.

4.3 Vertical distribution

Section 4.2 analyses the stellar distribution in the XY plane. In contrast, this section is devoted to analyse their vertical arrangement.

One way of comparing the southern ($b < 0°$) and the northern ($b > 0°$) parts of the Galactic disc, consist in splitting the pP30 sample into two bins: $-5° \leq b \leq 0°$ and $0° \leq b \leq 5°$. Then, their surface densities are computed as explained in Section 4.1.1, utilising, respectively, $(b_{min}, b_{max})_{b<0} = (-5, 0)°$ and $(b_{min}, b_{max})_{b>0} = (0, 5)°$. The resulting surface densities (imposing again $\delta l = 1°$ and $\Delta d = 100$ pc) are named $\Sigma_{b<0}$ and $\Sigma_{b>0}$ respectively.

In Fig. 5, their difference is normalised in relation to the uncertainty of the surface density of the full pP30 sample. That is, with respect to $\sigma[\Sigma]$, where Σ denotes those values plotted in Fig. 3. In turn, this uncertainty is roughly estimated by propagating a Poisson error for N equal to $\delta N \approx \sqrt{N}$. The employment of this relative deviation allows to highlight variations that are statistically representative in favour of those which are smaller than uncertainty fluctuations or of the same order. At the same time, $\sigma[\Sigma]$ introduces only small deviations to the general trend of $\Sigma_{b>0} - \Sigma_{b<0}$.

Fig. 5 reveals structures with discrepancies well beyond the 5σ level that cannot be explained by simple statistical fluctuations of the stellar density along the vertical direction. So, they originate in real differences in the observed stellar distribution. However, this may not necessarily correspond with the real one present in the Galaxy. Once again, extinction may affect the results. This is why the figure includes completeness limits for the $b < 0°$ and the $b > 0°$ subsamples, both computed as described in Section 4.2.1.

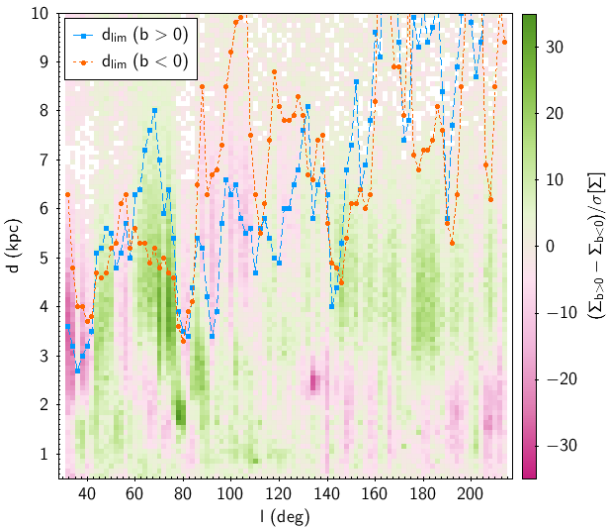

Fig. 5: Heliocentric distance versus Galactic longitude map of the difference between the surface densities for $b > 0°$ and $b < 0°$ relative to the uncertainty of the density of the full pP30 sample. Positive values mean larger densities in the northern bin. Completeness limits for the $b < 0°$ ($b > 0°$) subsamples are shown as circles (squares) connected by a dotted (dashed) line that guides the eye.

Despite they can only be treated qualitatively, a more in-depth analysis including the d_{lim} estimations of completeness limits provides to two important outcomes. First, it allows to detect differences in extinction between the northern and the southern disc. Second –and highly correlated with the previous one–, it provides a diagnostic to decide whether a feature in Fig. 5 has larger probability of being real or an artifact from detection limits due to differences in absorption between both subsamples. The following detailed, step-by-step, reasoning clarifies this statement.

Consider for instance the positive (green) patch

at $l \approx 70°$ in Fig. 5. Towards this direction, $d_{lim}(b > 0) > d_{lim}(b < 0)$, which implies that the sample can reach deeper distances for $b > 0°$. Therefore, extinction is higher for $b < 0°$ on average and thus, the number of stars included in a magnitude-limited catalogue would be smaller for $b < 0°$ –were stars are more faded– than for $b > 0°$. This directly results in the observed $\Sigma_{b>0}$ being larger than $\Sigma_{b<0}$ even if the real distribution of stars is completely homogeneous in this location. So, a positive value of $(\Sigma_{b>0} - \Sigma_{b<0})/\sigma[\Sigma]$ in this context may be caused by extinction biases –at least partially– rather than arising entirely from a real vertical peculiarity in the Galactic disc densities.

An analogous argument proves that the opposite stands when $d_{lim}(b > 0) < d_{lim}(b < 0)$ (as at $l \approx 100°$ or $l \approx 120°$ in Fig. 5).

For the same reason, $(\Sigma_{b>0} - \Sigma_{b<0})/\sigma[\Sigma]$ indicates a real density difference between both subsamples when $d_{lim}(b > 0) \approx d_{lim}(b < 0)$. For instance, this is the case for the positive (green) spot at $(l, d) \approx (80°, 1.75\,\mathrm{kpc})$ or the negative (pink) one at $(l, d) \approx (135°, 2.5\,\mathrm{kpc})$. The former may indicate that the Cygnus region is predominantly in the northern disc (as seen in the upper panel of figure 1 from Quintana & Wright 2021); even though, it is so close to a region with high extinction at $b < 0°$ that this value can also be partially artificial. While in contrast, the second example may suggest that the Perseus Arm diverts southwards or that there any other kind of stellar overdensity below the Galactic plane in this direction.

For the sake of completeness, median values of the Z_{Gal} coordinate for pP30 stars are plotted in Fig. 6. The sample is binned in l and d employing the same grid, with $\delta l = 1°$ and $\Delta d = 100\,\mathrm{pc}$. The colour code of this figure is set so that, as in Fig. 5, positive (green) values mean more stars observed at $b > 0°$.

Fig. 6 offers a lot of information. On the one hand, the range in Z_{Gal} of the closest bins to the Sun is extremely limited owing to the restriction in b of the sample. Therefore, their medians will always be systematically smaller than the furthest ones for this sample provided that the latter are not almost null. In any case, they can be examined with an analysis of structures with scales smaller than those on which this work is focused.

On the other hand, and as it is expected, it has features equivalent to those in Fig. 5, though they tend to start around $1 - 2\,\mathrm{kpc}$ later for median Z_{Gal} than for $(\Sigma_{b>0} - \Sigma_{b<0})/\sigma[\Sigma]$. The main examples of this are the positive (green) values at $60° \lesssim l \lesssim 80°$ and at $l \gtrsim 130°$, or the negative (pink) one between both of them. This demonstrates that both approaches are highly correlated. So, they lead to similar conclusions, and they are susceptible to the same biases as well.

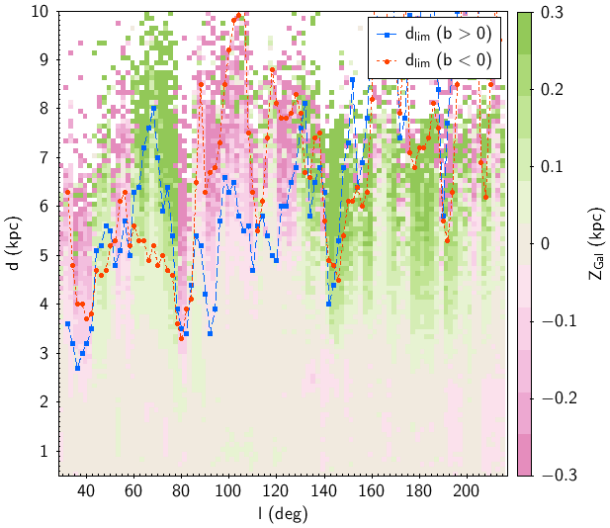

Fig. 6: Heliocentric distance versus Galactic longitude map of the distribution of median values of Z_{Gal} for the pP30 sample. See text for details about the grid. Positive values mean that stars are mostly at positive Z_{Gal}. Completeness limits for the $b < 0°$ ($b > 0°$) subsamples are shown as circles (squares) connected by a dotted (dashed) line to guide the eye.

5 Kinematics

So far I have discussed the Galactic structure as shown by the sample of A0-A5 stars. This section changes the subject and focuses on their kinematics.

As it has been said before, thanks to the intermediate age of A-type stars, they are kinetically cold. In other words, they have small intrinsic velocity dispersion (around 20 km/s according to Aumer & Binney 2009; Harris et al. 2018, 2019). In consequence, they are able to trace the original kinematic perturbations derived, for instance, from non-axisymmetric features of the Milky Way (e.g., spiral arms, the warp or bar resonances, among others) or from external interactions (as the Magellanic Clouds or the Sagittarius Dwarf galaxy).

Despite this, the lack of line-of-sight velocities for the sample (less than 1%) prevents the performance of a study of the full 3D velocity space aside from in very specific conditions. A non-exhaustive list of these exceptions is: towards the AC (where in good measure $\mathrm{V_R} \parallel \mathrm{v_{los}}$, $\mathrm{V}_\phi \parallel -\mathrm{v_l}$ and $\mathrm{V_Z} \parallel \mathrm{v_b}$), in the vertical direction using $\mathrm{V_Z} \equiv \mathrm{v_b^{corr}}$ (see Section 5.1 for issues with this approach) or imposing severe assumptions on the rotation curve of the Galaxy. The WEAVE spectrograph will help fulfill this $\mathrm{v_{los}}$ demand.

This section establishes and analyses some models and then compares the samples with them to discuss the observations.

5.1 Models and biases

Line-of-sight velocities needs spectroscopy to be measured. As this technique is typically very time-

consuming, its absence is usual even if it is a variable of high interest. Because of its lack, it is required to utilise a certain number of assumptions, which will possible generate some biases. They need to be taken into account so, two simple models are analysed in order to understand them.

The first model (hereinafter named Model 1) is based on a grid in (l, b, d) covering all Galactic longitudes in steps of 1°, having the same range $|b| \leq 5°$ than the sample with 0.1° intervals, and reaching up to $d = 10\,\mathrm{kpc}$ with a grid-spacing of 0.2 kpc. Their velocities are forced to circular orbits ($\mathrm{V_{R,\,Model}} = 0\,\mathrm{km/s}$) and to a flat rotation curve with $\mathrm{V_{\phi,\,Model}} = 240\,\mathrm{km/s}$ (Huang et al. 2016). It has no vertical velocities; that is, all points of the grid have $\mathrm{V_{Z,\,Model\,1}} = 0\,\mathrm{km/s}$. This model is used to examine global trends in the XY plane not directly involving vertical movements.

The second model (referred to as Model 2 from now on) is defined exactly as Model 1 with the only exception of vertical velocities. Instead of neglecting them, Model 2 has vertical oscillations with velocity amplitude $|\mathrm{V_{Z,\,Model\,2}(Z_{Gal})}| = \mathrm{V_{Z,0}\,sech^2(Z_{Gal}/Z_0)}$. The scale height Z_0 is chosen to be 200 pc as in Eq. (6), and the maximum modulus $\mathrm{V_{Z,0}}$ equals 10 km/s to be comparable with the dispersion in vertical velocities found by Gaia Collaboration et al. (2021a). The orientation of this motion is assigned randomly for each point of the grid. This representation of Model 2 does not intend to reproduce in detail the real kinematics of the Milky Way. Instead, it is applied to enable the study of vertical biases.

The results from these simulations described below will be compared with observational data in Sections 5.2 and 5.3.

The $\mathrm{v_{los}}$ distribution across the XY plane predicted by Model 1 is shown in Fig. 7. It can be easily explained by considering the relative approach or recession with respect to the Sun of a star orbiting at $R < R_\odot$ or $R > R_\odot$. To keep in mind that in this model the Galaxy rotates as a solid body can help in this visualization.

The essence of this figure is in perfect agreement with the quadrupole observed in the bottom panel of figure 5 from Katz et al. (2022), which show the sky distribution of *Gaia* DR3 line-of-sight velocities.

The transformation from heliocentric velocities $(\mathrm{v_l^{uncorr}}, \mathrm{v_b^{uncorr}}, \mathrm{v_{los}})$ into Galactocentric $(\mathrm{V_R}, \mathrm{V_\phi}, \mathrm{V_Z})$ leads to strong biases when $\mathrm{v_{los}}$ is missing. A commonly used approximation is to consider that $\mathrm{v_b^{corr}}$ is similar to $\mathrm{V_Z}$ for stars with small enough Galactic latitudes, as b and Z_{Gal} are almost parallel in this case. However, the projection of the true $(\mathrm{V_R}, \mathrm{V_\phi}, \mathrm{V_Z})$ in the b direction has a term that depends on $\mathrm{V_R}$ and $\mathrm{V_\phi}$ apart from the one proportional to $\mathrm{V_Z cos}(b)$. As proven by Croswell et al. (1987) in their figure 4, this additional component makes $\mathrm{v_b^{corr}}$ a low-accuracy estimator of $\mathrm{V_Z}$ whose fidelity changes with $\mathrm{V_R}$ and $\mathrm{V_\phi}$, as well as with the three-dimensional position within the Galaxy.

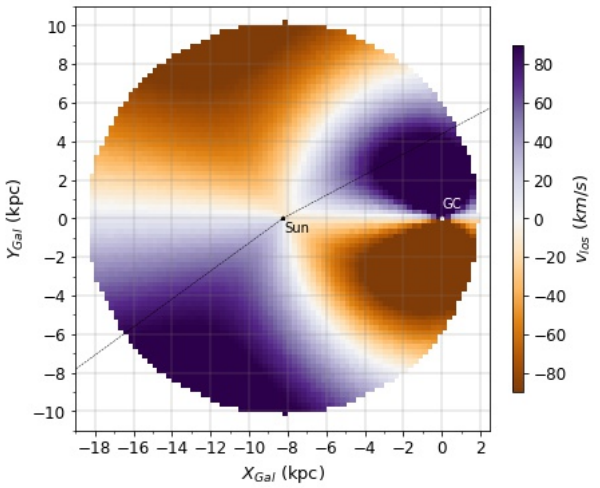

Fig. 7: Galactocentric XY map of uncorrected line-of-sight velocities derived from Model 1. The colour scale shows the median of what would be the observed $\mathrm{v_{los}}$. The GC is at the origin and the Sun is centred on the plot. Each bin has 0.25 kpc sides. Black diagonal lines show the Galactic longitude limits of the sample.

The last part of this section is dedicated to analyse how $\mathrm{v_b^{corr}}$ behaves in comparison with the real $\mathrm{V_Z}$ utilising Model 2. That is, to study the biases that are included when assuming $\mathrm{v_b^{corr}} \equiv \mathrm{V_Z}$. To do so, the proper motion in Galactic latitude is computed from the specified modelled velocity field and it is then corrected for solar motion according to Eq. (2).

As $\mathrm{V_{Z,\,Model\,2}}$ values have a randomly assigned sign, statistically half of the points will move northwards and the other half, southwards. For this reason, the median values of both $\mathrm{V_Z}$ and $\mathrm{v_b^{corr}}$ across the XY plane are null on average. To quantify their discrepancy, the median of the magnitude $|\mathrm{v_b^{corr}} - \mathrm{V_Z}|$ is used. Fig. 8 shows its distribution.

For a set of stars having perfectly circular orbits around the GC –like those in Model 2–, the line-of-sight velocity at exactly $l = 0°$ and $l = 180°$ is null. Thus, towards the GC and the AC, the three-dimensional space velocity can be fully recovered with no more than proper motions. This is why no deviations are found there, neither in Fig. 8 nor in the right panel of Fig. 9. Additionally, Fig. 8 proves that $|\mathrm{v_b^{corr}} - \mathrm{V_Z}|$ discrepancies grow when increasing $|l - 180°|$ following a non-trivial pattern that has two singularities because of the combination of a spherical and a cylindrical reference systems.

For a maximum $\mathrm{V_Z}$ imposed to be of the order of $\mathrm{V_{Z,0}} = 10\,\mathrm{km/s}$, median divergences reach up to $\sim 12\,\mathrm{km/s}$. That is, for instance, $\mathrm{v_b^{corr}}$ can double $\mathrm{V_Z}$ or even change its sign. Consequently, the assumption $\mathrm{v_b^{corr}} \equiv \mathrm{V_Z}$ can become extremely biased away from the AC, the GC or the plane $b = 0°$ (where b and

Z_{Gal} are completely parallel). The exact range of $|v_b^{corr} - V_Z|$ and the shape of its XY pattern slightly depends on ($U_\odot$, $V_\odot$, $W_\odot$), even if there are no appreciable changes when varying it within acceptable values.

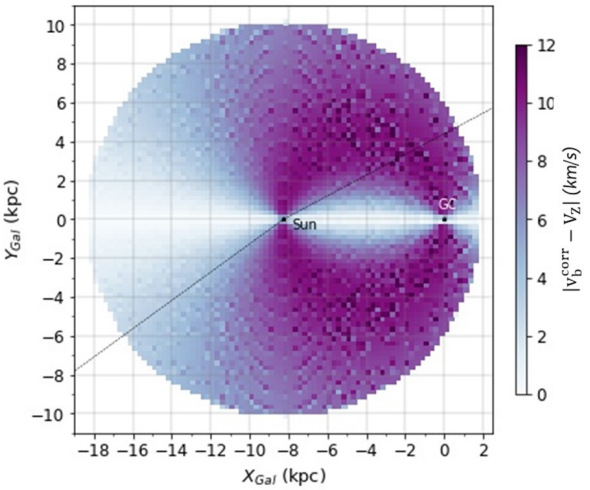

Fig. 8: XY map of median differences between v_b^{corr} and V_Z in absolute value obtained with Model 2. The GC is at the origin of coordinates and the Sun is centred on the plot. Bins are squares of side 0.25 kpc. Black diagonal lines show the Galactic longitude limits of the sample.

In addition to its Galactic longitude dependency, $v_b^{corr} - V_Z$ is also highly dependent on Z_{Gal}. In other words, this bias changes when getting away from the Galactic plane. Since this dependence is symmetric with respect to the Galactic plane ($Z_{Gal} = 0$), it is compensated when averaging over all Z_{Gal} inside bins in the XY plane (naturally, except when considering absolute values as in Fig. 8). However, vertical asymmetries in stellar density (e.g., due to extinction) would make this effect relevant because of the non-uniform sampling.

In general, this effect tends to create unreal compression or expansion effects that are not present in V_Z. Moreover, their magnitude obviously depends on l, as can be seen in Fig. 9. A detailed inspection of the v_b^{corr} dependence on Z_{Gal} and on l with Model 2 leads to the conclusion that v_b^{corr} displays an artificial compression breathing mode at $0° \lesssim l \lesssim 180°$ and an expansive one for the other half of the sky (i.e., $180° \lesssim l \lesssim 360°$) for any heliocentric distance.

Fig. 9 demonstrates this effect for two particular slices in Galactic longitude that are of special interest for the observational sample (see Section 5.2). Both cuts are chosen so that they have the same width in l, being defined as $60° \leq l \leq 75°$ and $172.5° \leq l \leq 187.5°$. The former encompasses a kinetically peculiar structure found in Fig. 10 (analysed in Section 5.2); whereas the latter is symmetric around the AC and proves that this is a privileged direction where $v_b^{corr} \equiv V_Z$ is verified.

In conclusion, using v_b^{corr} as the substitute of V_Z should be treated with care, always verifying that trends found cannot be reproduced by the biases.

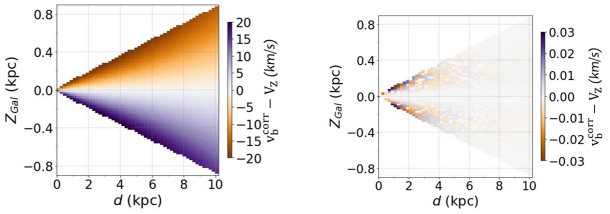

(a) $60° \leq l \leq 75°$ **(b)** $172.5° \leq l \leq 187.5°$

Fig. 9: Vertical Galactic coordinate as a function of heliocentric distance, colour-coded by the median of the difference $v_b^{corr} - V_Z$ for Model 2. Panel (a) shows the slice between $60° \leq l \leq 75°$ while panel (b) contains grid points with $172.5° \leq l \leq 187.5°$. In both cases, the size of the bins is 0.2 kpc in d and 20 pc in Z_{Gal}. Notice that both colour scales have very different ranges.

5.2 *Gaia* EDR3 vertical velocities

The pP30 sample only has 1 652 stars with line-of-sight velocities (see Section 3). Owing to this scarce statistics and the fact that these hot stars should not have had v_{los} in *Gaia* DR2 (Katz et al. 2019), they are ignored in this section. The more recent DR3 provides almost 20 times this number so, v_{los} are addressed in Section 5.3. In contrast, the current section focuses in vertical velocities; particularly, it analyses v_b^{corr} in a similar way as it has been done in the second half of Section 5.1.

As the data is limited to $30° \lesssim l \lesssim 215°$, the main expected bias induced by the usage of v_b^{corr} rather than V_Z is a compression breathing mode dependent on l (see Section 5.1).

The distribution of v_b^{corr} across the Galactocentric XY plane is shown in Fig. 10. It has two clear peculiarities: the $v_b^{corr} > 0$ km/s band between $160° \lesssim l \lesssim 210°$ starting at $R \approx 13 - 14$ kpc (leftmost edge of the sample) and the very negative region around $(X_{Gal}, Y_{Gal}) \approx (-6, 6)$ kpc. Additionally, they correspond surprisingly well with patterns founds for median Z_{Gal} (Fig. 6). This high correlation indicates that both the densities and the kinematic perturbations could have a common origin.

Fig. 10 shows the existence of a large-scale structure moving upwards that is located at large Galactocentric radii, approximately around the AC. This was also found by Romero-Gómez et al. (2019) with their OB sample; as well as with the one of RGB stars, even if it gets closer to the CG in this case. In addition, it is also recovered by the Gaia Collaboration et al. (2022a) RGB sample, which can use V_Z thanks to the new DR3 line-of-sigh velocities (their OB sample has an extremely limited extension and does not reach the required distances).

This feature is associated with the Galactic warp.

As it has been already said, it is located relatively close to the AC, at directions where the difference between v_b^{corr} and V_Z does not exceed 5 km/s according to Fig. 8. Assuming that deviations found in Model 2 are representative enough for the observational data, this structure is not compatible with these portion of the Milky Way having null vertical velocities. In consequence, Fig. 10 demonstrates the existence of a warp in the Milky Way.

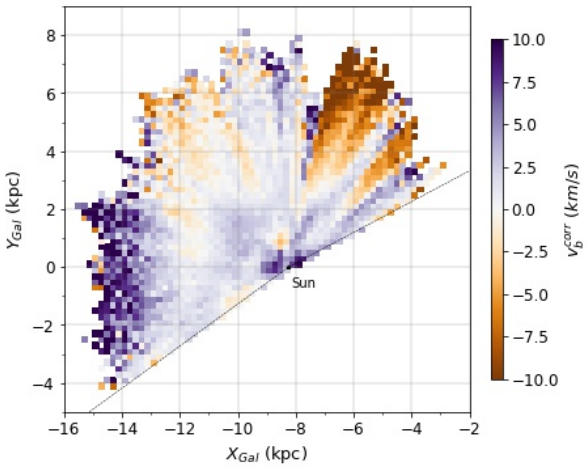

Fig. 10: Galactocentric XY map of the corrected velocities in the b direction from EDR3 proper motions of the pP30 sample. Bins have sides equal to 0.2 kpc and are colour-coded by the median of v_b^{corr}. Only those bins with 10 or more stars are shown. Black diagonal lines showing the Galactic longitude limits of the sample are the same as that in the plots of Section 5.1.

A galactic warp causes orbits of stars to have a specific vertical waving. In particular, figure 5.1 from Abedi (2015) shows that its maximum and minimum vertical velocities are reached towards the line-of-nodes for the case of a symmetric warp (to compare different warp geometries, see for instance Romero-Gómez et al. 2019). Furthermore, the amplitude of this oscillating motion is expected to grow with Galactocentric radius R, as so it does the maximum vertical coordinate reached (see, for instance, references in this paragraph).

Fig. 11 confirms this predictions by showing v_b^{corr} as a function of ϕ for different bins in Galactocentric radius. The furthest bins present larger dispersion because of their lower statistics. When comparing it with Fig. 10, it is worth to keep in mind that $l = 180°$ corresponds with $\phi = 0°$, that they belong to reference systems with different origins (i.e., l depends on ϕ, R and $R_\odot$) and that they grow in opposite directions (ϕ clockwise and l counterclockwise).

The smallest v_b^{corr} values beyond $\phi \approx 50°$ correspond with the $v_b^{corr} < 0$ km/s feature found in Fig. 10 at $(X_{Gal}, Y_{Gal}) \approx (-6, 6)$ kpc —or, equivalently, at $(l, d) \approx (60 - 75°, 6 - 7\,\mathrm{kpc})$—. Although this trend can be originated up to some extend by a local perturbation, it is likely to be an artifact derived from the combination of two biases: on the one hand, it is situated in a region of the XY plane were the bias of v_b^{corr} described in Section 5.1 is already relevant. On the other hand, it is observed towards a direction where nearby extinction is more concentrated below $b = 0°$ than above. This is easily deduced, for instance, from the difference between both completeness distances d_{lim} from Fig. 5 (Section 4.3), in figures 3-4 from Sale et al. (2014) or also in figure 2 from Green et al. (2019).

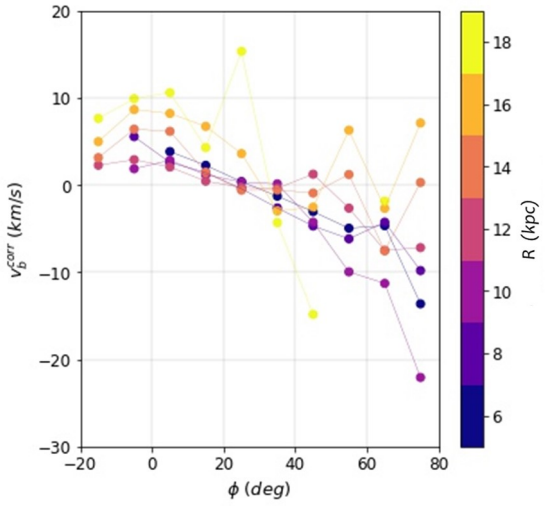

Fig. 11: Velocity in the b direction, corrected for the solar motion, versus the Galactocentric azimuthal coordinate. The pP30 sample sources are binned in R every 2 kpc.

The union of both effects is what creates this drop in median v_b^{corr}. High extinction at $b < 0°$ is responsible of the fact that detected stars are predominantly at $b > 0°$. At the same time, the bias described in Section 5.1 provokes that stars with $b > 0°$ have negative v_b^{corr}. As a result, averaged values of this variable in the XY plane are also negative.

To analyse this region in depth, two slices in l have been selected from the pP30 sample; namely $60° \leq l \leq 75°$ and $172.5° \leq l \leq 187.5°$ (as it has been done for Model 2 in Fig. 9). Fig. 12 shows how v_b^{corr} is distributed in the Z_{Gal}-d plane for each of them.

Fig. 12a shows a noticeable compression breathing mode that is very similar in amplitude to the one presented in 9a (note that these two panels cover almost the same auxiliary axis). A relevant difference between Model 2 and the pP30 sample is that the former displays a straight division between positive and negative velocities (thanks to its high degree of symmetry), while the band satisfying $v_b^{corr} \approx 0$ km/s seems to bends towards negative Z_{Gal} from $d \gtrsim 3.5$ kpc for pP30.

By contrast, Fig. 12b exhibits globally positive medians of v_b^{corr} caused by the Galactic warp. Furthermore, it also shows a compression breathing

mode, although much weaker than the previous one. Since this slice is centred in the AC, where $v_b^{corr} \equiv V_Z$ remains valid[6], this breathing mode could be real. At least, Fig. 9b does not show any similar bias for the same range of Galactic longitudes. However, it can also be a bias analogous to the aforementioned one caused by non-zero values of V_R (i.e., by stellar orbits being not perfectly circular).

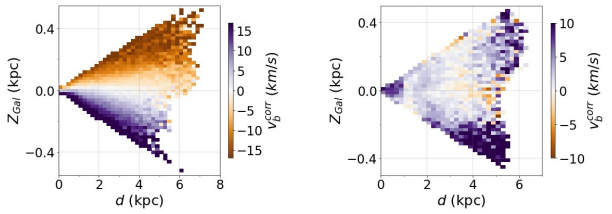

(a) $60\,^\circ \leq l \leq 75\,^\circ$ **(b)** $172.5\,^\circ \leq l \leq 187.5\,^\circ$

Fig. 12: Vertical Galactic coordinate as a function of the heliocentric distance, colour-coded by the median v_b^{corr} for the pP30 sample. Panel (a) displays the slice between $60° \leq l \leq 75°$ whereas panel (b) uses stars with $172.5° \leq l \leq 187.5°$. Bins sizes are the same as in Fig. 9, but notice that the range of the three axes are adapted to each sample. Bins with less than 10 stars are not shown.

5.3 *Gaia* DR3 line-of-sight velocities

Thanks to the new *Gaia* DR3, the number of stars in the sample having line-of-sight velocities has significantly grown. Although their absolute number (32 032 sources) still represents a very small fraction of the full sample, it is enough to compute kinematic maps for v_{los} and for each (V_R, V_ϕ, V_Z) component.

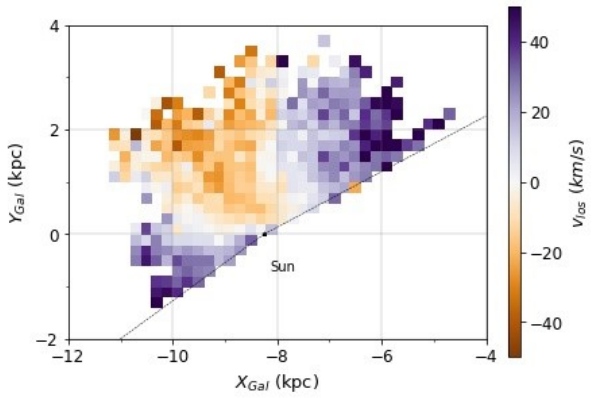

Fig. 13: Observed heliocentric line-of-sight velocity map in the Galactocentric XY plane for the pP30-DR3RV subsample. Each bin contains at least 10 stars and covers a square of 0.2 kpc in size. Black lines showing the Galactic longitude limits of the sample are the same as that in figures from Section 5.1.

For the sake of consistency, the same cut in parallax errors as before is applied, leading to the pP30-DR3RV sample (described in Section 3). Velocity maps with or without this quality cut are essentially the same when plotting only those bins containing a certain minimum number of sources. Moreover, by doing this, resulting maps have less random fluctuations at the largest distances and so, they are clearer.

The distribution of observed v_{los} across the XY plane is shown in Fig. 13. It basically exhibits the same pattern as predicted by Fig. 7.

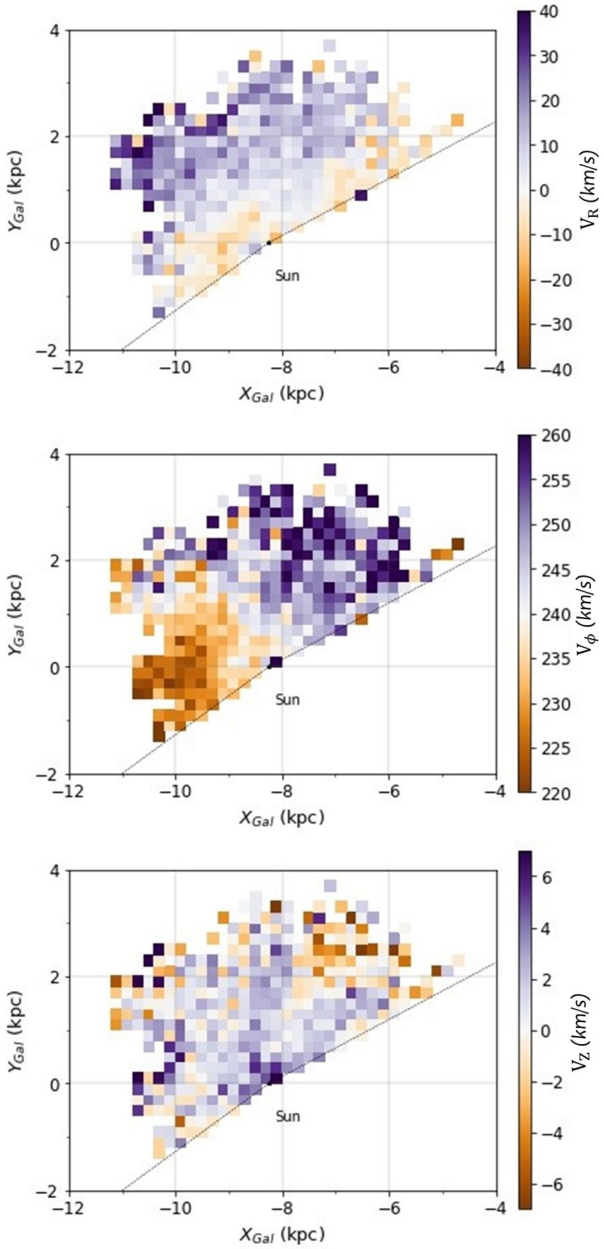

Fig. 14: Velocity maps of the pP30-DR3RV sample in the XY plane. They show medians of radial V_R, azimuthal V_ϕ and vertical V_Z velocities from top to bottom. The bins have 0.2 kpc per side, and only those containing 10 or more stars are shown. Black lines showing the Galactic longitude limits of the sample are the same as in all previous cases.

[6]In fact, for a sample covering $|b| \leq 5°$ towards the AC, $v_b^{corr} \gtrsim 0.996 V_Z$ as long as stars have no significant radial motions V_R.

Concerning the (V_R, V_ϕ, V_Z) Galactocentric components, their velocity maps in the XY plane are shown in Fig. 14. First, radial velocities are generally positive (around $l \approx 90°$ and in the second quadrant) except for two clumps close to the sample lower borders. Extension of the sample to the southern hemisphere will help to disentangle if they are part of larger structures. Second, the azimuthal ones are around 240 km/s in the solar vicinity and they seem to grow with ϕ. This map has lower values towards the AC and clearly larger values in the first quadrant.

Last, clear patterns and substructure are hard to recognise in vertical velocities. Moreover, Galactic warp effects are expected to start too far to be observed with this reduced sample. The most striking feature of this V_Z map is that it still shows the region with downwards motion ($V_Z < 0$ km/s) at $l \approx 60 - 75°$ that had been previously attributed –at least partially– to biases (see Fig. 10 and discussion in Section 5.2). Since the bottom panel in Fig. 14 uses V_Z instead of v_b^{corr}, it should be free from the aforementioned biases and thus, this negative vertical velocities could indeed be real. A more detailed analysis of this region will be done in the future.

It should be added that some of the detected features could be related with spiral arms. However, the small region covered, and the lack of part of the first and the third quadrants, as well as the full fourth quadrant, make it difficult to reach any conclusion in this regard.

6 Discussion

This section is devoted to discuss the major findings of the work, to contrast density and kinematics of A0-A5 stars with different tracers and to compare the results of this report with the literature. It follows the same order as the work, starting by density structures and then discussing the kinematics of the sample.

Regarding density structures, all points enumerated in Section 4.2 (see list in page 8) agree remarkably well with the overdensities and underdensities found by Poggio et al. (2021) in their figure 1. According to their results, the most likely assignation of these features are: a) small portion of the Perseus Arm; b), c) and e) different parts of the Local Arm; and f) the largest-l component of the Sagittarius-Carina Arm.

In contrast, when comparing with the left panel of figure 5 from Pantaleoni González et al. (2021), one can link c) and the first two peaks defined in e) with what they label as the Cepheus spur.

The low density reported in d) seems to arise naturally from the inter-arm region between the Perseus and the Local Arms based on the Poggio et al. (2021) approach. On the contrary, Cantat-Gaudin et al. (2020) highlights, in the same coordinates, a lack of open clusters that splits their more tightly wound model of the Perseus Arm (see the right panel of their figure 11). Regardless of which pitch angle is the correct one, the presence of an *empty* volume[7] at this position is clear. Furthermore, it is also recovered with the OB sample of Gaia Collaboration et al. (2022a), in their figures 12-14.

The three figures in Section 4.2 (namely, surface density and overdensity maps in Fig. 2, 3 and 4) correlate considerably well with the OB sample in figures 12 and 13 from Gaia Collaboration et al. (2022a). The main differences are that their OB sample has high densities at their $(x, y) \approx (0.5, 0.75)$ instead of showing a prominent overdensity in the Cygnus region. That is, their feature is located at a lower ϕ along their Local Arm. Moreover, when comparing Fig. 4 from this work with their figure 13, even the two radial positive overdensities starting at $(X, Y) \approx (-0.75, 3)$ kpc and at $(X, Y) \approx (-3, 1)$ kpc are comparable. This claims that there can be some real structure even if their exact distance is uncertain owing to the radial stretching.

Consider now the vertical distribution of the sample (Fig. 6 in Section 4.3). Despite of the difference in coordinates projection, it shows high agreement with both panels of figure 5 from Romero-Gómez et al. (2019); which use a sample of OB stars and one of RGB.

A very recognisable feature is the positive region around $l \approx 60 - 75°$, which is clearly shown in their two samples as well as in the pP30 one of this work. The largest positive region at $l \gtrsim 130°$ that starts after $d \approx 4$ kpc (e.g., covering a wide field-of-view around the AC beyond $R \approx 12$ kpc) also seems to agree with a combination of both OB and RGB samples from Romero-Gómez et al. (2019). It seems to be shifted in l with respect to the latter while it samples a larger area than the former. The negative clump at $80 \lesssim l \lesssim 130°$ corresponds better with the OB sample of the aforementioned authors than with their RGB sample, although they coincide for those Galactic longitudes nearer to $l = 90°$. Consequently, A-type stars seems to show some features detected both with younger and older stars, even if the exact distribution is highly dependent on the age of the tracer.

All previous results prove the high potential to reveal Galactic structures that has the used sample of A0-A5 stars. It allows to unveil density structures of the Milky Way that can be associated with spiral arms, as well as vertical patterns inside the Galactic disc (either real or caused by extinction and other biases). On the other hand, it is also very powerful for kinematic purposes, as Section 5 shows.

[7] At least, it is depleted of Upper Main Sequence stars (Poggio et al. 2021), A-type stars (this work) and open clusters (Cantat-Gaudin et al. 2020).

The vertical distribution of the pP30 sample is highly correlated with its v_b^{corr} map (see Fig. 6 and 10). Thus, they may be showing the combination of effects derived from similar physics as well as from interconnected biases.

An unexpected region with $v_b^{corr} < 0\,km/s$ found at $(X_{Gal}, Y_{Gal}) \approx (-6, 6)\,kpc$ in Fig. 10 has been analysed in Section 5.2. It has been attributed to the combination between extinction effects and the bias derived from considering $v_b^{corr} \equiv V_Z$. Its extension to larger heliocentric distances was also found with OB and RGB stars by Romero-Gómez et al. (2019), whose proper motions in b are referred to the LSR instead of to the Sun.

Maps of vertical velocity V_Z (so, free from bias in this case) from Gaia Collaboration et al. (2022a) do not show any peculiarity in these coordinates for RGB stars, whereas their OB sample is restricted to $d < 2\,kpc$. Nevertheless, the V_Z map of the pP30-DR3RV sample shown in the bottom panel of Fig. 14 does present a similar feature. Moreover, the upper-left panel of figure 23 from the same authors display two regions having compression breathing mode (negative values of their ΔV_Z). One of them is just the controversial location mentioned in the previous paragraph, whereas the other one is nearly symmetric around the AC and starts at $R \approx 11\,kpc$. Thus, even if there can still exist some residual biases, it is possible that the Milky Way disc is being partially compressed in some regions.

On the other hand, results shown in Fig. 14 can be compared with velocity maps for OB and RGB stars from Gaia Collaboration et al. (2022a). The gradient found in the pP30-DR3RV V_ϕ map is considerably similar to that of the middle left panel of figure 21 from these authors (which uses OB stars). It could be compared with their sample of RGB stars if their colour axis had a much narrower range.

The match is not so clear neither for V_R nor for V_Z. The former disagrees a lot with their RGB sample, while the leftmost negative feature is similar to that of their OB stars. On the other hand, this second sample has a band with positive vertical velocities between their coordinates $(x, y) \approx (-1, -0.5)$ and $(x, y) \approx (0, 1)$ which is only barely visible at the corresponding coordinates $(X_{Gal}, Y_{Gal}) = (x - R_\odot, y)$ of the bottom panel of Fig. 14 from this work.

The difference in the area of the Galactic plane covered by these three samples (namely, the pP30-DR3RV one and the two from Gaia Collaboration et al. 2022a) complicates their visual comparison. Furthermore, the Galactic latitude limit of the pP30-DR3RV sample highly reduces the statistics very close to the Sun. By contrast, the sample of A0-A5 stars reaches a little bit deeper than the one of OB stars. Complementing current data with the southern Galactic plane and with WEAVE line-of-sight velocities will highly improve these velocity maps.

Despite this, the strengths of A-type stars can be further exploited by analysing the velocity space asymmetries as it was done by Gaia Collaboration et al. (2021a) in their figure 13 (see also McMillan et al. 2022, which analyses these perturbations with a sample of blue stars). The approach consists in studying the density in the V_Z-V_ϕ plane, which displays several overdensities whose shape and size (and even their number in some cases) depend on R as well as on Z_{Gal}.

The number of A0-A5 stars in the pP30 sample is very large. However, the current study requires to use narrow Galactocentric radial bins and so, the pP50 and pP50-DR3RV samples are used here to improve the statistics to a greater extend (see Section 3 for the definition of these samples). As in Section 5.3, the effect of this cut in parallax error on the sample with *Gaia* DR3 line-of-sight velocities is negligible.

Gaia Collaboration et al. (2021a) use the approximations $V_Z \equiv v_b^{corr}$ and $V_\phi \equiv v_l^{corr}$ for a sample of sources (without any selection on stellar types) restricted to $170° \leq l \leq 190°$ and $|b| \leq 10°$. As pP50 does not have line-of-sight-velocities, the same cut in Galactic longitude ($170° \leq l \leq 190°$) has been applied and the same approximation is considered. On the other hand, since v_{los} information is very relevant to disentangle the origin of these inhomogeneities, I try to reproduce these results using V_ϕ and V_Z velocities for the entire pP50-DR3RV sample.

The first two rows of each panel of Fig. 15 compares the original plot from Gaia Collaboration et al. (2021a) with the distributions found with the pP50 sample, proving that found asymmetries agree without a doubt in most of the cases. They are also highly in agreement with the results at the AC shown in figure 7 from McMillan et al. (2022). The pP50 sample clearly show the aforementioned asymmetries with more well-defined clumpy regions. Furthermore, it traces these densities with a higher degree of detail, revealing some substructure previously unseen. Therefore, A-type stars are very useful to detect kinematic perturbations as well.

However, the number of A-type stars with *Gaia* DR3 line-of-sight velocities is too small and so, these asymmetries cannot be recovered with the pP50-DR3RV sample. Moreover, stars with large R are too dispersed in their velocity maps to obtain any conclusion from them and thus, they are not included in Fig. 15. To recover, at least partially, the large statistics of the original sample and complete these last panels, v_{los} measurements from WEAVE will be crucial. In contrast with *Gaia*, whose line-of-sight velocities methods are more focused on colder stars, WEAVE will have a survey specially dedicated to A-type stars (Jin et al. *in prep.*). Thus, it will definitely help filling this gap.

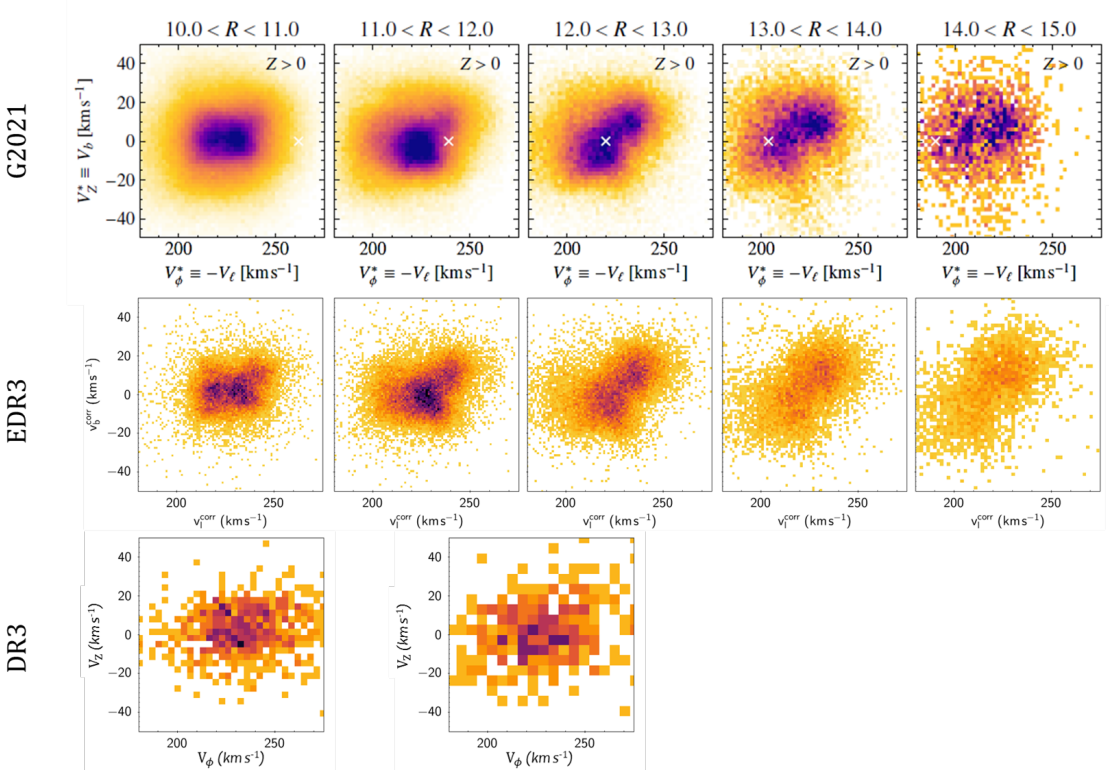

(a) $Z_{Gal} > 0$

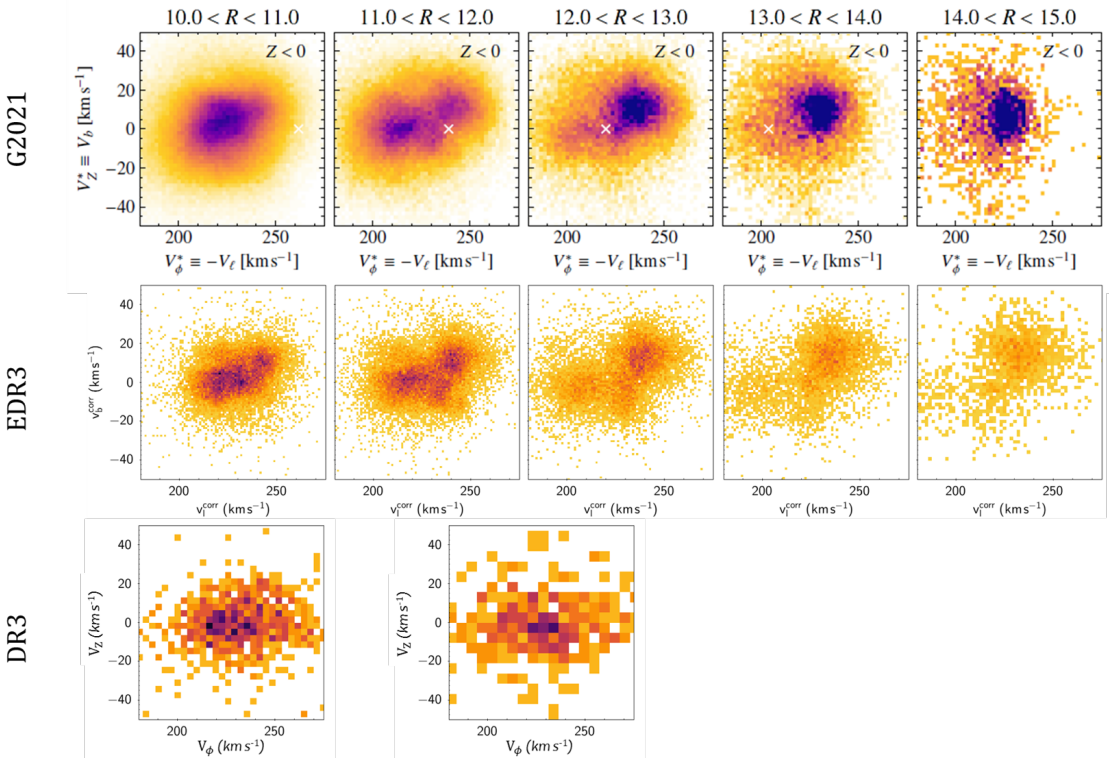

(b) $Z_{Gal} < 0$

Fig. 15: Density in the V_Z vs V_ϕ velocity maps for several Galactocentric radial bins distinguishing between $Z_{Gal} > 0$ (three rows above) and $Z_{Gal} < 0$ (three rows below). The colour scale is in the sense that darker means denser. Its range is the same for each pair of rows with different Z_{Gal}, but changes between different samples. Bin sizes have been adapted to the number of stars of each panel (between 339 and 29213 for results from this work). In each case, the upper row (G2021) is the corresponding section of figure 13 from Gaia Collaboration et al. (2021a), the middle one (EDR3) shows the results from the pP50 sample and the bottom row (DR3) presents the pP50-DR3RV data. Bins in R are the same for G2021 and EDR3 rows; while for the DR3 one, they are $10.0 < R < 11.0$ in the left panel and $11.0 < R < 13.0$ in the right one.

7 Conclusions and future work

A sample of A0-A5 stars selected with a colour-colour diagram from IGAPS photometric bands has been used to unveil Milky Way density structures and kinematic perturbations.

The surface densities shown in Fig. 3 and the Fig. 4 overdensity map enable the detection of a portion of the Perseus arm, the Cygnus region, a low-density region at $(X, Y) \approx (-1.75, 0.5)\,\mathrm{kpc}$, a high-density area that may be associated with the Cepheus Spur and other small density peaks near the AC. The strength of radial features created by extinction and distance uncertainties is diminished when applying quality cuts in parallax errors. Structures found with a sample reduced using this restriction have been verified and agree with the literature.

On the other hand, the study of the vertical distribution of stellar densities has been done with Fig. 5. It proves that many of the prominent differences between $b > 0°$ and $b < 0°$ are introduced by extinction and may not entirely correspond with real asymmetric distributions. However, a detailed analysis of the completeness of each half of the sample is needed to determine up to which distance this figure is reliable at each Galactic longitude. As expected, results from median Z_{Gal} in Fig. 6 are in general highly correlated with the previous ones.

Two simple models have been used to determine which biases can be introduced by the lack of line-of-sight velocities. The main conclusion from this part of the study is that the $\mathrm{v_b^{corr}} \equiv \mathrm{V_Z}$ approximation needs to be treated with care. It is verified near the AC provided that stellar orbits have negligible Galactocentric radial motion ($\mathrm{V_R} \approx 0\,\mathrm{km/s}$). However, $\mathrm{v_b^{corr}}$ and $\mathrm{V_Z}$ can be extremely discrepant towards other Galactic longitudes. In addition, this bias has a strong dependence on the vertical coordinate Z_{Gal} that creates artificial breathing modes on observational data. When this effect is combined with non-uniform extinction, it can create kinematic peculiarities as the one visible in Fig. 10 around $(X_{Gal}, Y_{Gal}) \approx (-6, 6)\,\mathrm{kpc}$.

Besides this, the same figure shows a clear evidence of the Galactic warp as a large-scale substructure moving upwards in the XY plane. When analysed as a function of R, larger Galactocentric radius have higher $\mathrm{v_b^{corr}}$ velocities at a given Galactocentric azimuth ϕ, which corresponds with theoretical predictions.

A first overview on line-of-sight velocities from *Gaia* DR3 exhibits the basic expected trends. However, the reliable range of distances of kinematic maps is very small owing both to the sample limit in b (which highly diminishes the number of sampled stars for $d \lesssim 1\,\mathrm{kpc}$) and to the maximum distance reached by the pP30-DR3RV sample.

This works demonstrates the strength of A-type stars as tracers of structure and kinematics, as well as the importance of obtaining the full 6D phase space information.

Some extra analyses that can be performed on the sample are shown as examples of work currently in progress that will be further investigated. On the one hand, Galactocentric velocity maps across the XY plane are shown in Fig. 14; while on the other, the capability of the sample as a tracer of kinematic perturbations in the outer Galactic disc is highlighted in Fig. 15.

More examples of future work that can be performed with this type of samples are:

- Further exploit advantages of A-type stars by expanding the sample to the southern Galactic plane using VPHAS, the IGAPS counterpart in the south. Or, as an additional possibility, using synthetic photometry from *Gaia* DR3 to apply the same selection explained in Section 3 and obtain an homogeneous all-sky sample of A0-A5 stars.

- Refine the completeness analysis simulating the effects and biases caused by each one of the cuts that are applied to the sample, as briefly stated at the end of Section 4.2.1. As well as estimating with more detail the contamination fraction of the sample.

- Enlarge the number and the limiting magnitude of stars having line-of-sight velocities using future observations from the WEAVE spectrograph.

- Take advantage of A-type stars to study large-scale dynamics of the Milky Way or kinematic properties and patterns in star-forming regions, among others.

To conclude, A-type stars are extremely powerful tracers that can be used in addition to those historically used to complete and increase our knowledge about the properties and the evolution of the Milky Way as a galaxy.

Acknowledgements

I would like to express my sincere gratitude to my advisor for her invaluable advice and her support in every sense. In addition, I would like to thank Dr. Francesca Figuras, Dr. Luis Aguilar, Dr. Mercè Romero and Dr. Teresa Antoja, along with all the UB Gaia team for their scientific discussions and comments that helped improving this work. I am also grateful to David Altamirano for the exchanges of ideas and some programming codes we have had. I appreciate as well the unconditional support of my family and my friends, who always believe in me.

This work made use of TOPCAT[8] and STILTS[9] Visual Observatory tools.
This research made use of Astropy,[10] a community-developed core Python package for Astronomy (Astropy Collaboration et al. 2013, 2018).
This work has made use of data from the European Space Agency (ESA) mission *Gaia* (https://www.cosmos.esa.int/gaia), processed by the *Gaia* Data Processing and Analysis Consortium (DPAC, https://www.cosmos.esa.int/web/gaia/dpac/consortium). Funding for the DPAC has been provided by national institutions, in particular the institutions participating in the *Gaia* Multilateral Agreement.

References

Abedi, H. 2015, PhD thesis, University of Barcelona, Spain

Amôres, E. B., Robin, A. C., & Reylé, C. 2017, A&A, 602, A67

Antoja, T., Helmi, A., Romero-Gómez, M., et al. 2018, , 561, 360

Astraatmadja, T. L. & Bailer-Jones, C. A. L. 2016, ApJ, 832, 137

Astropy Collaboration, Price-Whelan, A. M., Sipőcz, B. M., et al. 2018, The Astronomical Journal, 156, 123

Astropy Collaboration, Robitaille, T. P., Tollerud, E. J., et al. 2013, A&A, 558, A33

Aumer, M. & Binney, J. J. 2009, MNRAS, 397, 1286

Bailer-Jones, C. A. L. 2015, Publications of the Astronomical Society of the Pacific, 127, 994

Bailer-Jones, C. A. L., Rybizki, J., Fouesneau, M., Demleitner, M., & Andrae, R. 2021, The Astronomical Journal, 161, 147

Belokurov, V., Erkal, D., Evans, N. W., Koposov, S. E., & Deason, A. J. 2018, MNRAS, 478, 611

Blomme, R., Fremat, Y., Sartoretti, P., et al. 2022, arXiv e-prints, arXiv:2206.05486

Cantat-Gaudin, T., Anders, F., Castro-Ginard, A., et al. 2020, A&A, 640, A1

Chen, X., Wang, S., Deng, L., et al. 2019, Nature Astronomy, 3, 320

Croswell, K., Latham, D. W., & Carney, B. W. 1987, The Astronomical Journal, 93, 1445

Dalton, G. 2016, in Astronomical Society of the Pacific Conference Series, Vol. 507, Multi-Object Spectroscopy in the Next Decade: Big Questions, Large Surveys, and Wide Fields, ed. I. Skillen, M. Balcells, & S. Trager, 97

Drew, J. E., Greimel, R., Irwin, M. J., et al. 2005, MNRAS, 362, 753

Drew, J. E., Greimel, R., Irwin, M. J., & Sale, S. E. 2008, MNRAS, 386, 1761

Drimmel, R. & Poggio, E. 2018, Research Notes of the American Astronomical Society, 2, 210

Gaia Collaboration, Antoja, T., McMillan, P. J., et al. 2021a, A&A, 649, A8

Gaia Collaboration, Brown, A. G. A., Vallenari, A., et al. 2021b, A&A, 649, A1

Gaia Collaboration, Drimmel, R., Romero-Gomez, M., et al. 2022a, arXiv e-prints, arXiv:2206.06207

Gaia Collaboration, Prusti, T., de Bruijne, J. H. J., et al. 2016, A&A, 595, A1

Gaia Collaboration, Vallenari, A., Brown, A., T., P., & et al. 2022b, A&A

Gravity Collaboration, Abuter, R., Amorim, A., et al. 2020, A&A, 636, L5

Green, G. M., Schlafly, E., Zucker, C., Speagle, J. S., & Finkbeiner, D. 2019, ApJ, 887, 93

Groot, P. J., Verbeek, K., Greimel, R., et al. 2009, MNRAS, 399, 323

Harris, A., Drew, J. E., Farnhill, H. J., et al. 2018, MNRAS, 475, 1680

Harris, A., Drew, J. E., & Monguió, M. 2019, MNRAS, 485, 2312

Helmi, A., Babusiaux, C., Koppelman, H. H., et al. 2018, , 563, 85

Huang, Y., Liu, X. W., Yuan, H. B., et al. 2016, MNRAS, 463, 2623

Katz, D., Sartoretti, P., Cropper, M., et al. 2019, A&A, 622, A205

Katz, D., Sartoretti, P., Guerrier, A., et al. 2022, arXiv e-prints, arXiv:2206.05902

Lallement, R., Vergely, J. L., Babusiaux, C., & Cox, N. L. J. 2022, A&A, 661, A147

Luri, X., Brown, A. G. A., Sarro, L. M., et al. 2018, A&A, 616, A9

[8] http://www.star.bris.ac.uk/~mbt/topcat/
[9] http://www.star.bris.ac.uk/~mbt/stilts/
[10] http://www.astropy.org

McMillan, P. J., Petersson, J., Tepper-Garcia, T., et al. 2022, arXiv e-prints, arXiv:2206.04059

Monguió, M., Greimel, R., Drew, J. E., et al. 2020, A&A, 638, A18

Monguió, M., Grosbøl, P., & Figueras, F. 2015, A&A, 577, A142

Pantaleoni González, M., Maíz Apellániz, J., Barbá, R. H., & Reed, B. C. 2021, MNRAS, 504, 2968

Poggio, E., Drimmel, R., Cantat-Gaudin, T., et al. 2021, A&A, 651, A104

Quintana, A. L. & Wright, N. J. 2021, MNRAS, 508, 2370

Reid, M. J. & Brunthaler, A. 2020, ApJ, 892, 39

Romero-Gómez, M., Mateu, C., Aguilar, L., Figueras, F., & Castro-Ginard, A. 2019, A&A, 627, A150

Sale, S. E., Drew, J. E., Barentsen, G., et al. 2014, MNRAS, 443, 2907

Sale, S. E., Drew, J. E., Knigge, C., et al. 2010, MNRAS, 402, 713

van der Kruit, P. C. & Searle, L. 1981, A&A, 95, 105